Intensity-based modified Doppler variance algorithm: application to phase instable and phase stable optical coherence tomography systems

Gangjun Liu,[1,2] Lidek Chou,[1] Wangcun Jia,[1] Wenjuan Qi,[1] Bernard Choi,[1,2] and Zhongping Chen[1,2,*]

[1]*Beckman Laser Institute, University of California, Irvine, Irvine, California 92612, USA*
[2]*Department of Biomedical Engineering, University of California, Irvine, Irvine, California 92697, USA*
*z2chen@uci.edu

Abstract: The traditional phase-resolved Doppler method demonstrates great success for in-vivo imaging of blood flow and blood vessels. However, the phase-resolved method always requires high phase stability of the system. In phase instable situations, the performance of the phase-resolved methods will be degraded. We propose a modified Doppler variance algorithm that is based on the intensity or amplitude value. Performances of the proposed algorithm are compared with traditional phase-resolved Doppler variance and color Doppler methods for both phase stable and phase instable systems. For the phase instable situation, the proposed algorithm demonstrates images without phase instability induced artifacts. *In-vivo* imaging of window-chamber hamster skin is demonstrated for phase instable situation with a spectrometer-based Fourier domain OCT system. A microelectromechanical systems (MEMS) based swept source OCT (SSOCT) system is also used to demonstrate the performance of the proposed method in a phase instable situation. The phase stability of the SSOCT system is analyzed. In-vivo imaging of the blood vessel of human skin is demonstrated with the proposed method and the SSOCT system. For the phase stable situation, the proposed algorithm also demonstrates comparable performance with traditional phase-resolved methods. *In-vivo* imaging of the human choroidal blood vessel network is demonstrated with the proposed method under the phase stable situation. Depth-resolved fine choroidal blood vessel networks are shown.

© 2011 Optical Society of America

OCIS codes: (170.4500) Optical coherence tomography; (170.3890) Medical optics instrumentation; (170.3340) Laser Doppler velocimetry.

References and links

1. D. Huang, E. A. Swanson, C. P. Lin, J. S. Schuman, W. G. Stinson, W. Chang, M. R. Hee, T. Flotte, K. Gregory, C. A. Puliafito, and J. G. Fujimoto, "Optical coherence tomography," Science **254**(5035), 1178–1181 (1991).
2. Z. Chen, T. E. Milner, D. Dave, and J. S. Nelson, "Optical Doppler tomographic imaging of fluid flow velocity in highly scattering media," Opt. Lett. **22**(1), 64–66 (1997), http://www.opticsinfobase.org/abstract.cfm?URI=ol-22-1-64.
3. Z. Chen, T. E. Milner, S. Srinivas, X. Wang, A. Malekafzali, M. J. C. van Gemert, and J. S. Nelson, "Noninvasive imaging of *in vivo* blood flow velocity using optical Doppler tomography," Opt. Lett. **22**(14), 1119–1121 (1997), http://www.opticsinfobase.org/ol/abstract.cfm?URI=ol-22-14-1119.
4. J. A. Izatt, M. D. Kulkarni, S. Yazdanfar, J. K. Barton, and A. J. Welch, "*In vivo* bidirectional color Doppler flow imaging of picoliter blood volumes using optical coherence tomography," Opt. Lett. **22**(18), 1439–1441 (1997), http://www.opticsinfobase.org/abstract.cfm?URI=ol-22-18-1439.
5. Y. Zhao, Z. Chen, C. Saxer, S. Xiang, J. F. de Boer, and J. S. Nelson, "Phase-resolved optical coherence tomography and optical Doppler tomography for imaging blood flow in human skin with fast scanning speed and

high velocity sensitivity," Opt. Lett. **25**(2), 114–116 (2000), http://www.opticsinfobase.org/abstract.cfm?URI=ol-25-2-114.

6. R. K. Wang, L. An, S. Saunders, and D. J. Wilson, "Optical microangiography provides depth-resolved images of directional ocular blood perfusion in posterior eye segment," J. Biomed. Opt. **15**(2), 020502 (2010).

7. Y. K. Tao, K. M. Kennedy, and J. A. Izatt, "Velocity-resolved 3D retinal microvessel imaging using single-pass flow imaging spectral domain optical coherence tomography," Opt. Express **17**(5), 4177–4188 (2009), http://www.opticsinfobase.org/abstract.cfm?uri=oe-17-5-4177.

8. L. An, H. M. Subhush, D. J. Wilson, and R. K. Wang, "High-resolution wide-field imaging of retinal and choroidal blood perfusion with optical microangiography," J. Biomed. Opt. **15**(2), 026011 (2010).

9. B. Vakoc, S. Yun, J. de Boer, G. Tearney, and B. Bouma, "Phase-resolved optical frequency domain imaging," Opt. Express **13**(14), 5483–5493 (2005), http://www.opticsinfobase.org/abstract.cfm?URI=oe-13-14-5483.

10. J. Barton and S. Stromski, "Flow measurement without phase information in optical coherence tomography images," Opt. Express **13**(14), 5234–5239 (2005), http://www.opticsinfobase.org/abstract.cfm?URI=oe-13-14-5234.

11. A. Mariampillai, B. A. Standish, E. H. Moriyama, M. Khurana, N. R. Munce, M. K. K. Leung, J. Jiang, A. Cable, B. C. Wilson, I. A. Vitkin, and V. X. D. Yang, "Speckle variance detection of microvasculature using swept-source optical coherence tomography," Opt. Lett. **33**(13), 1530–1532 (2008), http://www.opticsinfobase.org/abstract.cfm?URI=ol-33-13.

12. A. Mariampillai, M. K. K. Leung, M. Jarvi, B. A. Standish, K. Lee, B. C. Wilson, A. Vitkin, and V. X. D. Yang, "Optimized speckle variance OCT imaging of microvasculature," Opt. Lett. **35**(8), 1257–1259 (2010), http://www.opticsinfobase.org/abstract.cfm?URI=ol-35-8-1257.

13. Y. Yasuno, Y. J. Hong, S. Makita, M. Yamanari, M. Akiba, M. Miura, and T. Yatagai, "In vivo high-contrast imaging of deep posterior eye by 1-μm swept source optical coherence tomography and scattering optical coherence angiography," Opt. Express **15**(10), 6121–6139 (2007), http://www.opticsinfobase.org/abstract.cfm?URI=oe-15-10-6121.

14. E. Jonathan, J. Enfield, and M. J. Leahy, "Correlation mapping method for generating microcirculation morphology from optical coherence tomography (OCT) intensity images," J. Biophotonics, 4:n/a (2011), doi: 10.1002/jbio.201000103 *http://onlinelibrary.wiley.com/doi/10.1002/jbio.201000103/pdf*

15. Y. Zhao, Z. Chen, C. Saxer, Q. Shen, S. Xiang, J. F. de Boer, and J. S. Nelson, "Doppler standard deviation imaging for clinical monitoring of *in vivo* human skin blood flow," Opt. Lett. **25**(18), 1358–1360 (2000), http://www.opticsinfobase.org/abstract.cfm?URI=ol-25-18-1358.

16. H. Ren, K. M. Brecke, Z. Ding, Y. Zhao, J. S. Nelson, and Z. Chen, "Imaging and quantifying transverse flow velocity with the Doppler bandwidth in a phase-resolved functional optical coherence tomography," Opt. Lett. **27**(6), 409–411 (2002), http://www.opticsinfobase.org/abstract.cfm?URI=ol-27-6-409.

17. G. Liu, W. Qi, L. Yu, and Z. Chen, "Real-time bulk-motion-correction free Doppler variance optical coherence tomography for choroidal capillary vasculature imaging," Opt. Express **19**(4), 3657–3666 (2011), http://www.opticsinfobase.org/abstract.cfm?URI=oe-19-4-3657.

18. B. J. Vakoc, G. J. Tearney, and B. E. Bouma, "Statistical properties of phase-decorrelation in phase-resolved Doppler optical coherence tomography," IEEE Trans. Med. Imaging **28**(6), 814–821 (2009).

19. J. Zhang and Z. Chen, "In vivo blood flow imaging by a swept laser source based Fourier domain optical Doppler tomography," Opt. Express **13**(19), 7449–7457 (2005), http://www.opticsinfobase.org/abstract.cfm?URI=oe-13-19-7449.

20. M. Yamanari, Y. Lim, S. Makita, and Y. Yasuno, "Visualization of phase retardation of deep posterior eye by polarization-sensitive swept-source optical coherence tomography with 1-μm probe," Opt. Express **17**(15), 12385–12396 (2009), http://www.opticsinfobase.org/oe/abstract.cfm?URI=oe-17-15-12385.

21. B. Baumann, B. Potsaid, J. J. Liu, M. F. Kraus, D. Huang, J. Hornegger, J. S. Duker, and J. G. Fujimoto, "Retinal blood flow measurement with ultrahigh-speed swept-source / Fourier domain optical coherence tomography," Proc. SPIE **7885**, 78850H (2011), doi:10.1117/12.875672.

22. B. R. White, M. C. Pierce, N. Nassif, B. Cense, B. Park, G. Tearney, B. Bouma, T. Chen, and J. de Boer, "In vivo dynamic human retinal blood flow imaging using ultra-high-speed spectral domain optical coherence tomography," Opt. Express **11**(25), 3490–3497 (2003), http://www.opticsinfobase.org/oe/abstract.cfm?URI=OPEX-11-25-3490.

23. R. A. Leitgeb, L. Schmetterer, W. Drexler, A. F. Fercher, R. J. Zawadzki, and T. Bajraszewski, "Real-time assessment of retinal blood flow with ultrafast acquisition by color Doppler Fourier domain optical coherence tomography," Opt. Express **11**(23), 3116–3121 (2003), http://www.opticsinfobase.org/abstract.cfm?uri=oe-11-23-3116.

24. S. Makita, Y. Hong, M. Yamanari, T. Yatagai, and Y. Yasuno, "Optical coherence angiography," Opt. Express **14**(17), 7821–7840 (2006), http://www.opticsinfobase.org/abstract.cfm?URI=oe-14-17-7821.

25. L. An and R. K. Wang, "In vivo volumetric imaging of vascular perfusion within human retina and choroids with optical micro-angiography," Opt. Express **16**(15), 11438–11452 (2008), http://www.opticsinfobase.org/abstract.cfm?URI=oe-16-15-11438.

26. L. Yu and Z. Chen, "Doppler variance imaging for three-dimensional retina and choroid angiography," J. Biomed. Opt. **15**(1), 016029 (2010).

27. R. K. Wang, L. An, P. Francis, and D. J. Wilson, "Depth-resolved imaging of capillary networks in retina and choroid using ultrahigh sensitive optical microangiography," Opt. Lett. **35**(9), 1467–1469 (2010), http://www.opticsinfobase.org/abstract.cfm?URI=ol-35-9-.
28. J. Fingler, R. J. Zawadzki, J. S. Werner, D. Schwartz, and S. E. Fraser, "Volumetric microvascular imaging of human retina using optical coherence tomography with a novel motion contrast technique," Opt. Express **17**(24), 22190–22200 (2009), http://www.opticsinfobase.org/abstract.cfm?URI=oe-17-24-22190.
29. I. Grulkowski, I. Gorczynska, M. Szkulmowski, D. Szlag, A. Szkulmowska, R. A. Leitgeb, A. Kowalczyk, and M. Wojtkowski, "Scanning protocols dedicated to smart velocity ranging in spectral OCT," Opt. Express **17**(26), 23736–23754 (2009), http://www.opticsinfobase.org/abstract.cfm?uri=oe-17-26-23736.
30. S. Zotter, M. Pircher, T. Torzicky, M. Bonesi, E. Götzinger, R. A. Leitgeb, and C. K. Hitzenberger, "Visualization of microvasculature by dual-beam phase-resolved Doppler optical coherence tomography," Opt. Express **19**(2), 1217–1227 (2011), http://www.opticsinfobase.org/abstract.cfm?URI=oe-19-2-1217.
31. S. Makita, F. Jaillon, M. Yamanari, M. Miura, and Y. Yasuno, "Comprehensive in vivo micro-vascular imaging of the human eye by dual-beam-scan Doppler optical coherence angiography," Opt. Express **19**(2), 1271–1283 (2011), http://www.opticsinfobase.org/abstract.cfm?URI=oe-19-2-1271.
32. T. Fabritius, S. Makita, Y. Hong, R. Myllylä, and Y. Yasuno, "Automated retinal shadow compensation of optical coherence tomography images," J. Biomed. Opt. **14**(1), 010503 (2009).

1. Introduction

Optical coherence tomography (OCT) is a powerful interferometric technique to noninvasively obtain tissue cross section images with micrometer resolution, millimeter penetration depth and video-rate imaging speed [1]. The extension of the OCT technique to functionally image blood flow has generated great interests. Doppler optical coherence tomography (DOCT) or optical Doppler tomography (ODT) is one type of functional extension of OCT which combines the Doppler principle with OCT and provides in-vivo imaging of blood vessels, blood flow direction, and blood flow speed [2–5]. Phase-resolved Doppler OCT has become one of the favored methods for blood vessels imaging because of its high velocity sensitivity [5]. The method is based on the phase information obtained from complex OCT data. By analyzing the phase information, blood flow speed, blood flow direction, etc. can be obtained [5]. Optical microangiography (OMAG) is a type of DOCT extension that filters out the lower Doppler frequency component with numerical or hardware methods [6–8]. OMAG is sensitive to the phase term although it may not use the phase term directly.

The phase-resolved method is sensitive to the phase term, and phase stability of the OCT system is important for obtaining high quality images. The minimum velocity that can be resolved by the phase resolved method is determined by the phase stability of the OCT system. A dense beam scan will be required to provide the effective over sampling ratio and ensure phase correlation between adjacent A-lines [9]. Intensity-based methods have also been proposed to image blood vessels. Barton et al. proposed a method based on the speckle of conventional amplitude optical coherence tomography images [10]. Mariampillai et al. used the speckle variance in a small 3D volume to image blood vessels [11,12]. Yasuno et al. used the intensity threshold binarization-based method, scattering optical coherence angiography (SOCA), for retinal and choroidal blood vessel imaging [13]. SOCA does not need a dense scan as required by the phase resolved method and does not require a high phase stable system. However, the intensity threshold based method loses the functional information of blood flow, it is difficult for it to distinguish the flow signals from structure signals [8]. Jonathan et al. used a 2-D correlation map based on the OCT intensity images for blood vessel extraction [14].

The Doppler variance method is a method that uses the bandwidth of the Doppler frequency spectrum to image blood vessels [15]. Doppler variance has the advantages of being less sensitive to the pulsatile nature of the blood flow and the incident angle, as well as the capability of being used for quantifying the transverse flow velocity [16]. Doppler variance is not sensitive to gradient phase changes and can be used without bulk-motion-correction for *in-vivo* imaging [17]. In this paper, we modified the averaging Doppler variance algorithm to make it an intensity based method for blood vessel imaging. Intensity-based

methods do not require a phase stabilized system and can be used for a phase instable situation, such as a swept source Fourier domain OCT (FDOCT) system. Performances of the proposed algorithm are compared with traditional phase resolved Doppler variance and color Doppler (CD) methods for both phase stable and phase instable systems.

For the phase instable situation, the proposed algorithm demonstrates good results without phase instability induced artifacts. *In-vivo* imaging of window-chamber hamster skin is shown using a spectrometer-based FDOCT system under phase instable situation. A microelectromechanical systems (MEMS) based swept source OCT (SSOCT) system was also used to demonstrate the performance of the proposed method in a phase instable situation. The phase stability of the MEMS laser SSOCT system is analyzed. *In-vivo* imaging of the blood vessel of human skin is demonstrated with the proposed method. For the phase stable situation, the proposed algorithm also demonstrates comparable performance with the traditional phase resolved methods. *In-vivo* imaging of a human choroidal blood vessel network is demonstrated with the proposed method under the phase stable situation. Depth-resolved image of fine choroidal blood vessel network is shown.

2. Method

The algorithm to calculate Doppler variance is derived from autocorrelation technique [15,17]:

$$\sigma^2 = \frac{1}{T^2}\left(1 - \frac{\left|A_{j,z}A_{j+1,z}^*\right|}{A_{j,z}A_{j,z}^*}\right) \tag{1}$$

where $A_{j,z}$ is the complex data at *jth* A-line at depth of z and T is the time difference between adjacent A-lines. The algorithm is usually used with averaging to improve the signal to noise ratio (SNR) of the images. The averaging can be performed in lateral direction or in both lateral and axial directions [15,17]:

$$\sigma^2 = \frac{1}{T^2}\left[1 - \frac{\left|\sum_{j=1}^{J}\left(A_{j,z}A_{j+1,z}^*\right)\right|}{\sum_{j=1}^{J}\left(A_{j,z}A_{j,z}^*\right)}\right] \tag{2}$$

$$\sigma^2 = \frac{1}{T^2}\left[1 - \frac{\left|\sum_{j=1}^{J}\sum_{z=1}^{N}\left(A_{j,z}A_{j+1,z}^*\right)\right|}{\sum_{j=1}^{J}\sum_{z=1}^{N}\left(A_{j,z}A_{j,z}^*\right)}\right]. \tag{3}$$

It can be found that Eq. (1) is only related to the intensity or the amplitude of the complex data. When the averaging algorithms in Eq. (2) and Eq. (3) are used, the phase terms are also involved, and the values are affected by the adjacent A-line phase difference variance in the averaging area. Therefore, the variance values obtained by Eq. (2) and Eq. (3) are functions of both the amplitude and phase terms of the complex OCT data. The Doppler variance obtained with Eqs. (2) and (3) shows excellent results when the phase stability of the system is high. In the phase instable situation where there is phase jumping or jittering between adjacent A-lines, the variance value will be affected greatly by the abrupt change in phase terms. Here, we propose a modified averaging Doppler variance algorithm to eliminate the effect of the phase jumping. Instead of using Eqs. (2) and (3) for averaging, we used the modified averaging algorithm as follows:

$$\sigma^2 = \frac{1}{T^2}\left[1 - \frac{\sum\limits_{j=1}^{J}\left|\left(A_{j,z}A_{j+1,z}^*\right)\right|}{\sum\limits_{j=1}^{J}\left(A_{j,z}A_{j,z}^*\right)}\right] \tag{4}$$

$$\sigma^2 = \frac{1}{T^2}\left[1 - \frac{\sum\limits_{j=1}^{J}\sum\limits_{z=1}^{N}\left|\left(A_{j,z}A_{j+1,z}^*\right)\right|}{\sum\limits_{j=1}^{J}\sum\limits_{z=1}^{N}\left(A_{j,z}A_{j,z}^*\right)}\right]. \tag{5}$$

With the modified algorithm, all the phase terms will be cancelled out, and the resulting variance value is only related to the intensity or amplitude terms. The variance value obtained with Eqs. (4) and (5) is usually smaller than that obtained with Eqs. (2) and (3) because the phase variance is also taken into consideration when Eqs. (2) and (3) are used. Generally, larger J and N values in the algorithms will increase image SNR, however it also increases the computation time and decreases the resolution of the system. In this paper, we are using J = 4, N = 4 for lateral and depth averaging the images to balance between SNR and resolution. When Eq. (5) is used, the final variance value is multiplied by 3. In the following, Doppler variance method using Eq. (3) is called phase-resolved Doppler variance (PRDV), and Doppler variance method using Eq. (5) is called intensity-based Doppler variance (IBDV).

3. Application for phase instable OCT systems

3.1 Spectrometer-based FDOCT system

Spectrometer-based FDOCT systems usually show very good phase stability because no moving parts are used in the system. Most phase-sensitive techniques demonstrated are based on this kind of OCT systems. However, there are situations where the system phase stability degrades due to effects, such as vibration, galvanometer mirror scanner jittering [18]. Here, we demonstrate a special case where the phase stability of the system degrades due to galvanometer scanner jittering during scanning. The schematic diagram of the system setup is shown in Fig. 1. The spectrometer-based FDOCT uses a super luminescent diode (SLD) light source which has a central wavelength of 890 nm and full width at half maximum (FWHM) bandwidth of 150 nm. The CCD integration time was set at 50 µs. The system sensitivity was measured to be about 100 dB at around zero imaging depth. The 6-dB sensitivity roll-off distance was found to be at an imaging depth of 1.6 mm. The imaging process includes background signal subtraction, linear interpolation to convert data from the linear wavelength space to the linear wavenumber space, and numerical dispersion. The axial resolution was measured to be 3.5 µm. The phase stability of the system was measured to be 0.48 milliradians with a static mirror.
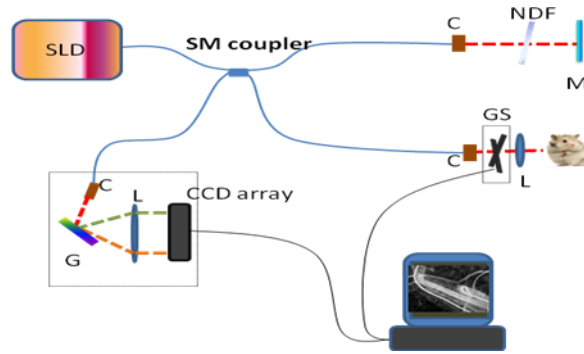
Fig. 1. Schematic of the spectrometer-based FDOCT system. SLD: Super luminescent diode; C: Collimator; NDF: Neutral density filter; M: Mirror; G: Grating; L: Lens; GS: Galvanometer mirror scanner.

A two-axis galvanometer mirror-based scanner was used to translate the imaging location. In this case, the galvanometer mirror-based scanner decreased the phase stability of the system and introduced phase jumping between adjacent A-lines. Figure 2 shows images of the skin of a dorsal window chamber installed hamster. Figures 2(a), 2(b), 2(c) and 2(d) show the OCT structure image, CD image, PRDV image and IBDV image, respectively. Figure 2(e) shows the zoomed image of the region in the white rectangle in Fig. 2(b). In Fig. 2(e), the phase difference values between $-\pi/3$ and $\pi/3$ are color-coded in a 256 grayscale image and the color bar is shown next to Fig. 2(e). The phase difference values larger than $\pi/3$ are expressed as red and the phase difference values smaller than $-\pi/3$ are expressed as blue in Fig. 2(e). Figure 2(f) shows the zoomed image for the region in the white rectangle in Fig. 2(c). From the CD images, the phase difference jumping can be seen at several locations as indicated by the red arrows. The phase instability affects the PRDV images more significantly, and the vertical lines in the images degrade the quality of the final results. With IBDV, the result shows great improvement as shown in Fig. 2(d). It should be noted that the image shown in Fig. 2(d) was obtained by multiplying 3 to the variance value determined by Eq. (5). This demonstrates that images obtained with Eqs. (2) and (3) will show better results when phase stability of the system is high. Traditional PRDV algorithms take both the amplitude and phase terms into consideration. The effect of the phase term dominates the results. However, the amplitude term also contributes to the results. By multiplying 3 to the final variance value when IBDV algorithm is used, the amplitude term contribution is amplified. The yellow arrows in Figs. 2(b), 2(c) and 2(d) indicate the locations of the blood vessels obtained with CD, PRDV and IBDV methods, respectively. All three methods are able to detect the three blood vessels. CD offers ability to quantify the flow information such as blood flow direction relative to the incident laser beam, and flow speed. PRDV and IBDV cannot provide the information such as flow direction and flow speed. However these two methods may provide better contrast for mapping vascular network in some cases. For example, the blood vessel indicated by left most yellow arrow in Fig. 2(b) is hard to be identified. However, this vessel can be clearly identified in Figs. 2(c) and 2(d).
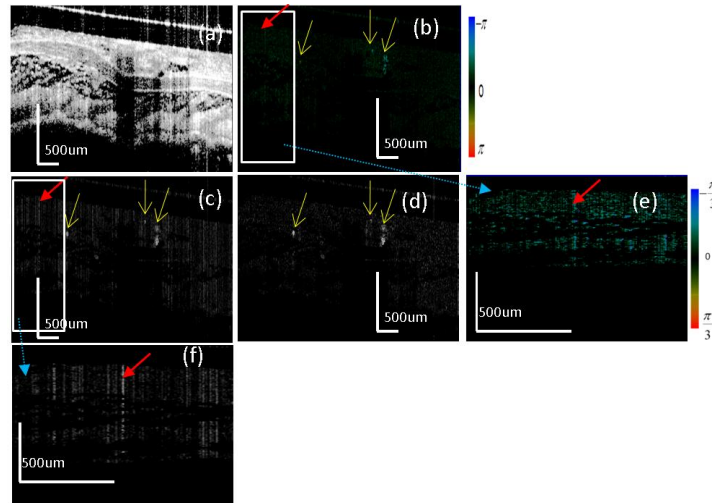
Fig. 2. (a) OCT structure image; (b) CD image; (c) PRDV image; (d) IBDV image. (e) Zoomed image for the region in the white rectangle in (b). (f). Zoomed image for the region in the white rectangle in (c).

3.2 Swept source FDOCT system

Swept source OCT (SSOCT) systems usually use tunable filters that are based on mechanically scanning of galvanometer mirror, polygon mirror or Fabry–Pérot (FP) filter. Due to the mechanical scanning schemes used, swept source OCT systems usually show worse phase stability than spectrometer-based OCT systems. If phase sensitive methods are used, phase correction must be done before using the phase-resolved algorithm [9,19–21]. We used a SSOCT system in this study. The schematic of the system setup is shown in Fig. 3. The system used a MEMS-based swept source laser with a central wavelength of 1310 nm, an A-line speed of 50 kHz and a total average power of 16 mW (SSOCT-1310, Axsun Technologies Inc, Billerica, MA). The system used a Mach-Zehnder type interferometer with 90% of the light in the sample arm and 10% of the light in the reference arm. A dual-balanced detection scheme was used to acquire the signal. The system utilizes K-trigger mode so that no re-calibration is needed. In order to analyze the phase stability of the SSOCT system, a static mirror was used as a sample, and phase differences between adjacent A-lines at the mirror location were obtained (Fig. 4). Figure 4(a) shows the phase difference distribution and Fig. 4 (b) shows the histogram of the phase difference distribution. Although the histogram as in Fig. 4(b) shows a Gaussian like profile with an FWHM value of 0.18 radians, there are still very significant counts of large phase differences. This can be seen more clearly from Fig. 4(a) which shows lots of phase jumping between adjacent A-lines.
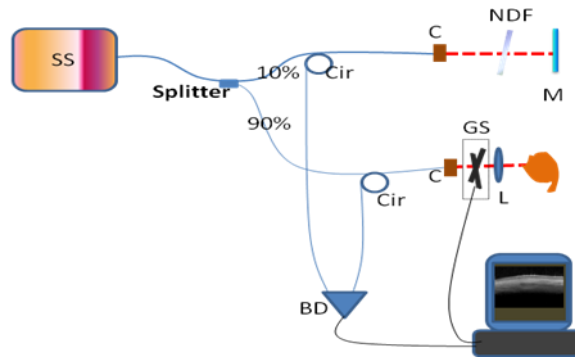
Fig. 3. Schematic of the swept source Fourier domain OCT system. SS: Swept source laser: C: Collimator; Cir: Circulator; NDF: Neutral density filter; M: Mirror; BD: Balanced detector; L: lens; GS: Galvanometer mirror scanner.
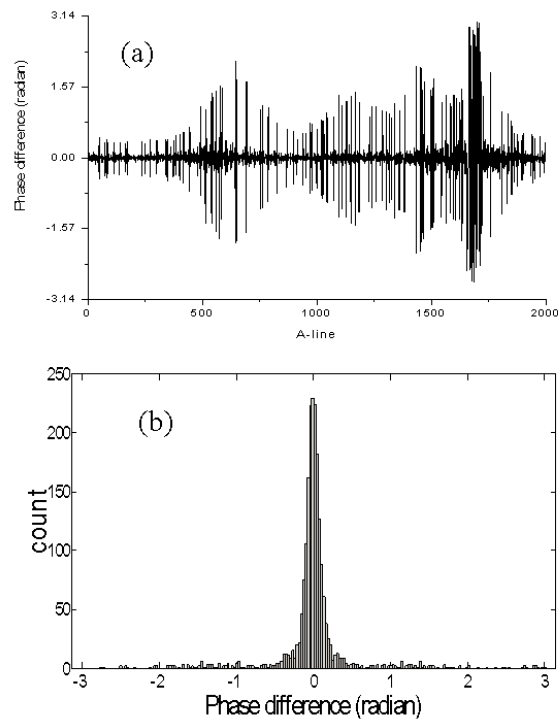

Fig. 4. Phase stability analysis of the SSOCT system. (a) Phase differences between adjacent A-lines at the static mirror location. (b). Histogram of the phase difference distribution.

Figure 5 shows the *in-vivo* images of human finger skin obtained with the SSOCT system. No phase correction method was used for CD and PRDV images. Figures 5(a), 5(b), 5(c) and 5(d) are, respectively, OCT structure, CD, PRDV and IBDV images. Figure 5(e) shows the zoomed image of the region in the white rectangle in Fig. 5 (b). In Fig. 5(e), the phase difference values between $-\pi/3$ and $\pi/3$ are color-coded in a 256 grayscale image and the color bar is shown next to Fig. 5(e). The phase difference values larger than $\pi/3$ are expressed in red and the phase difference values smaller than $-\pi/3$ are expressed in blue in Fig. 5(e). The yellow arrows in Figs. 5(b), 5(c) and 5(d) indicate the blood vessel. The CD image shown in Figs. 5(b) and 5(e) shows background that may be from the bulk phase

artifact induced by bulk motion, which was from involuntary finger movement during imaging. The bulk phase artifact degrades the image quality of the CD method, and the blood vessel indicated by the yellow arrow is not evident in this case. In addition, there are abrupt phase difference changes in the image as indicated by the red arrows. This was caused by the time jitter between adjacent A-line trigger signals shown in Fig. 4(a). This time jitter degrades the phase stability of the system, which degrades the quality of images obtained with the phase resolved method such as phase resolved CD and PRDV. This can be seen from Figs. 5(b) and 5(c). The CD images as shown in Figs. 5(b) and 5(e) show artifacts of vertical lines as indicated by the arrows. This indicates that the phase difference changes abruptly in the adjacent A-lines. More evident vertical lines exist in the Doppler variance image obtained with the phased resolved algorithm Eq. (3). These vertical line artifacts do not exist in the OCT structure image as in Fig. 5(a), which demonstrates that the vertical lines are coming from the phase terms. With the modified, intensity-based algorithm Eq. (5), the IBDV result as in Fig. 5(d) shows a much clearer image without any artifact.
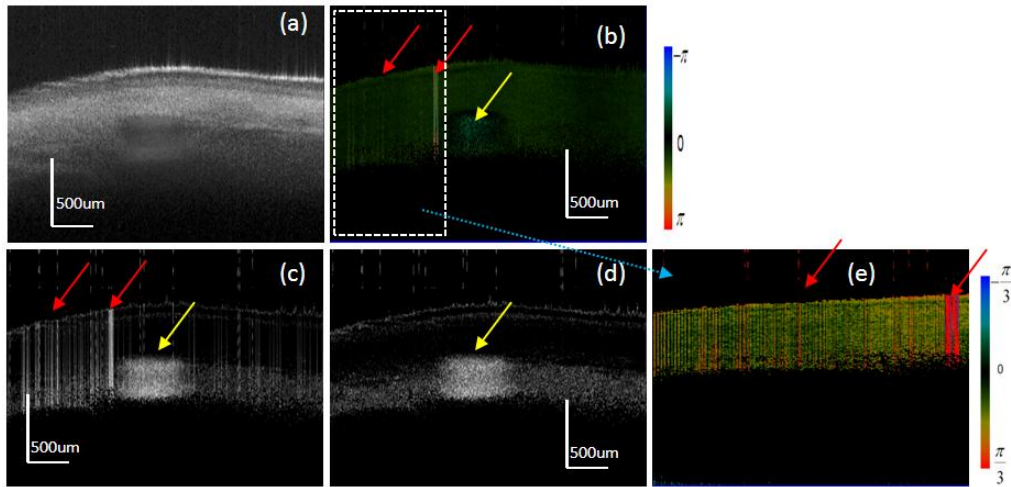

Fig. 5. (a) OCT structure image; (b) CD image; (c) PRDV image; (d) IBDV image. (e) Zoomed image of the region in the white rectangle in (b).

4. Application for phase stable OCT systems

In-vivo imaging of retinal and choroidal microvasculature is very interesting. Excellent blood vessel networks in the retina and choroid have been demonstrated with DOCT and its extended techniques. Phased-resolved DOCT and OMAG have been used to obtain high resolution blood vessel microvasculature [6–8,17,22–26]. For these phase-resolved methods, sensitivity can be further improved by increasing the time between adjacent A-lines. Without sacrificing the imaging speed, the algorithms have been used at inter-frame instead of inter-A-line, and ultrahigh sensitive performance has been demonstrated [27–29]. Recently, two probe beams with a certain delay between them have been used to obtain ultrahigh sensitive retinal and choroidal blood vessel microvasculature [30,31]. Intensity threshold binarization-based SCOA has been demonstrated for retinal and choroidal blood vessels imaging [13,32]. Although it is simple to implement, it has drawbacks as mentioned in the introduction section.

Here, we used the proposed intensity-based Doppler variance method for *in-vivo* imaging of retinal and choroidal vasculature. The imaging system is the same spectrometer-based OCT system as discussed in Section 3.1 except that a modified scanning head from a commercial Zeiss Stratus OCT is used here. The galvanometer mirror-based scanner in the scanning head shows much better phase stability in this case. The optical power of the beam on the corneal was set at 650 μW. The CCD integration time was set at 50 μs. Figure 6 shows the OCT

images of retina from a healthy volunteer. Figures 6(a), 6(b), 6(c) and 6(d) are, respectively, OCT structure, CD, PRDV and IBDV images. Each image contains 2048 A-lines and covers a scanning range of 5 mm.

The CD image [Fig. 6(b)] suffers from bulk motion artifacts caused by the involuntary head movement of the volunteer. The CD image shows great deal of background that degrades the performance of this method. Sample movement induced bulk motion should be corrected when CD method is used [8,16]. The PRDV image shown in Fig. 6(c) does not suffer from bulk motion artifacts and may be used without bulk motion removal [16]. As shown in the red circle regions in Figs. 6(c) and 6(d), the obtained IBDV result, is comparable to result obtained with the PRDV method. The yellow arrows in the red circles in Figs. 6(c) and 6(d) indicate the location of blood vessels detected. There vessels are not able to be resolved by the CD method without bulk motion correction. Both the PRDV and IBDV methods provide the better results than CD method in this case. The IBDV algorithm is, however, simple and solely intensity or amplitude based.
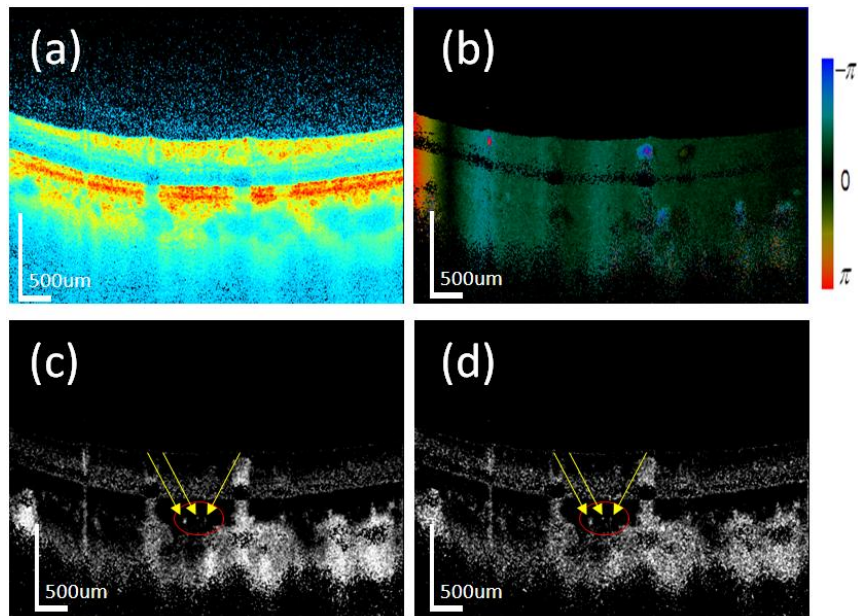

Fig. 6. (a) OCT structure image; (b) CD image; (c) Doppler variance image obtained with Eq. (3); (d) Doppler variance image obtained with modified algorithm Eq. (5).

The growing interest of using OCT to image the retina and choroid is because of its depth-resolved capability. Depth-resolved imaging of blood vessel network using OCT has been demonstrated with OMAG and OCA techniques [6,26,31]. In this paper we demonstrated that, with the IBDV, a fine blood vessels network down to the choroidal layers can be obtained. Figures 7(a)–7(k) show the depth-resolved en-face Doppler variance images obtained with the IBDV algorithm. The whole 3D volume includes 120 frames with 2048 A-lines per frame. Each en-face image covers a region of 5 mm by 5 mm. Figures 7(a)–7(k) show, respectively, the en-face images at a depth of 18.5 μm, 37 μm, 55.5 μm, 74 μm, 92.5 μm, 111 μm, 129.5 μm,148 μm,166.5 μm, 185 μm, 203.5 μm below the RPE layer. Figure 7(l) shows the projection view of the Doppler variance images obtained by summing all of the en-face Doppler variance images below the RPE layer. From the projection view image in Fig. 7(l), we are able to see the whole blood vessel networks below the RPE layer in one signal image.
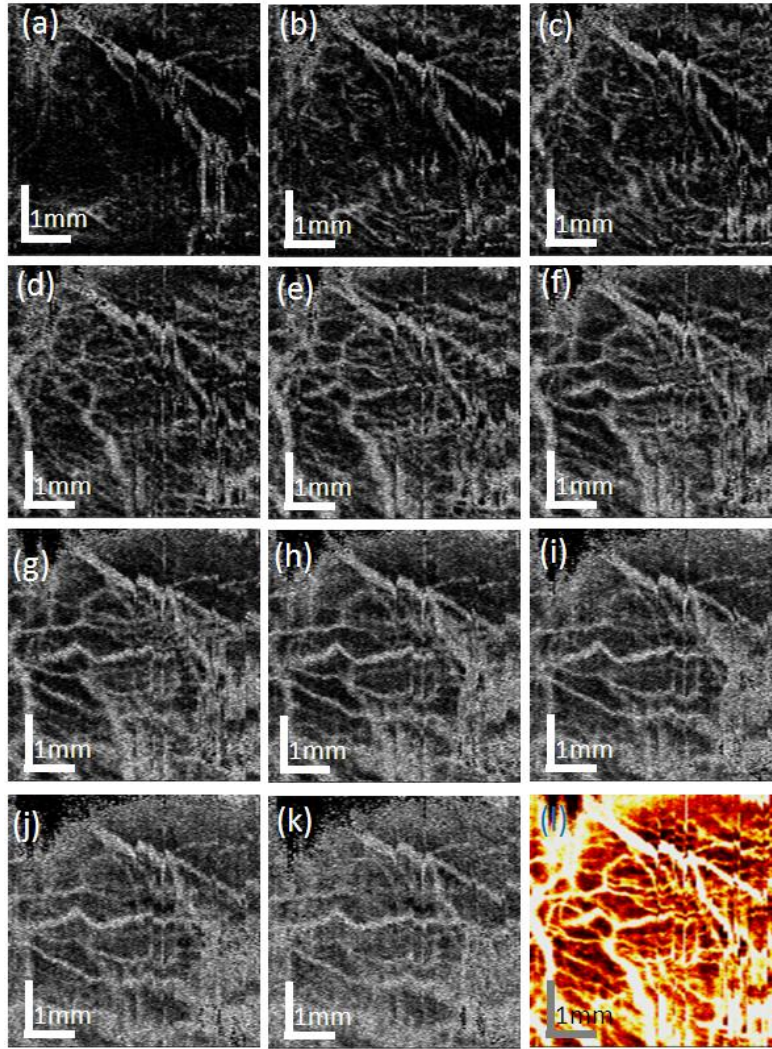
Fig. 7. En-face and projection view IBDV images. (a)–(k) are depth-resolved en-face IBDV images. (a)–(k) are, respectively, at a depth of 18.5 μm, 37 μm, 55.5 μm, 74 μm, 92.5 μm, 111 μm, 129.5 μm, 148 μm, 166.5 μm, 185 μm, 203.5 μm below the RPE layer. The depth difference between adjacent images is 18.5 μm. (l) Projection view of the IBDV image for all layers below the RPE layer.

5. Conclusions

In conclusion, we proposed a modified algorithm to calculate the Doppler variance. The modified algorithm is based on the intensity or amplitude value and not related to phase terms. Performances of the proposed algorithm were compared with traditional Doppler variance and CD methods for two phase instable systems. The proposed algorithm demonstrated good performance without phase instability induced artifacts in a phase instable situation. Two phase instable systems, a spectrometer-based FDOCT system and a SSOCT system, were used to demonstrate this. In the phase stable situation, the proposed algorithm demonstrated comparable results with the phase-resolved ODT and Doppler variance methods. Depth resolved chorioidal blood vessels microvasculature obtained with the proposed method was also demonstrated.

Acknowledgments